

# Asymmetrical coffee rings from cellulose nanocrystals and prospects in art and design

Konrad W. Klockars  · Noora E. Yau · Blaise L. Tardy  · Johanna Majoinen ·  
Tero Kämäräinen  · Kati Miettunen  · Elisa Boutonnet · Maryam Borghei  ·  
Jaana Beidler · Orlando J. Rojas 

Received: 5 September 2018 / Accepted: 28 November 2018 / Published online: 18 December 2018  
© The Author(s) 2018

**Abstract** The iridescence displayed by films made from cellulose nanocrystals (CNCs) has long been the subject of fundamental research. This has expanded our understanding of colloidal self-assembly towards the development of advanced materials. However, the application of such findings is less reported for visual designs that exploit structural color. Aesthetic outputs are already in reach, but requires input from trend setters in the design and art industries. In this realm, the CNC-based iridescence uniquely offers broadband, multi-colored reflections through the “coffee ring” effect, which arises upon evaporation-induced self-assembly (EISA). Although this effect has been thoroughly studied in the context of axisymmetric patterns, complex geometries remain to be evaluated for large-scale

implementation. This is central to the present efforts, where EISA of CNC suspensions occurred onto non-circular surfaces. We used orientation-dependent contact angle measurements, profilometry and fixed-light source photography to unveil the effect of asymmetric drying fluxes at sharp angles, between 30° and 90°, on CNC particle deposition and resulting color patterns. We also demonstrate the causality between increased capillary fluxes and deposition with the help of modelling via energy minimization of the suspension volume onto a given surface and using the diffusion equation to obtain the local concentration of water vapor during EISA. Lastly, we study the effect of background reflections as well as light and temperature resistance of CNC-based reflectors, both important for any deployment. The results from this multidisciplinary effort, involving applied design, art and colloid chemistry, point to the excellent prospects of CNC films for the development of structured and chromatic patterns.

---

Konrad W. Klockars and Noora E. Yau equally contributed to this paper.

---

**Electronic supplementary material** The online version of this article (<https://doi.org/10.1007/s10570-018-2167-7>) contains supplementary material, which is available to authorized users.

---

K. W. Klockars · N. E. Yau · B. L. Tardy ()  
J. Majoinen · T. Kämäräinen · K. Miettunen ·  
M. Borghei · O. J. Rojas (  
Department of Bioproducts and Biosystems, School of Chemical Engineering, Aalto University, 00076 Aalto, Finland

e-mail: blaise.tardy@aalto.fi

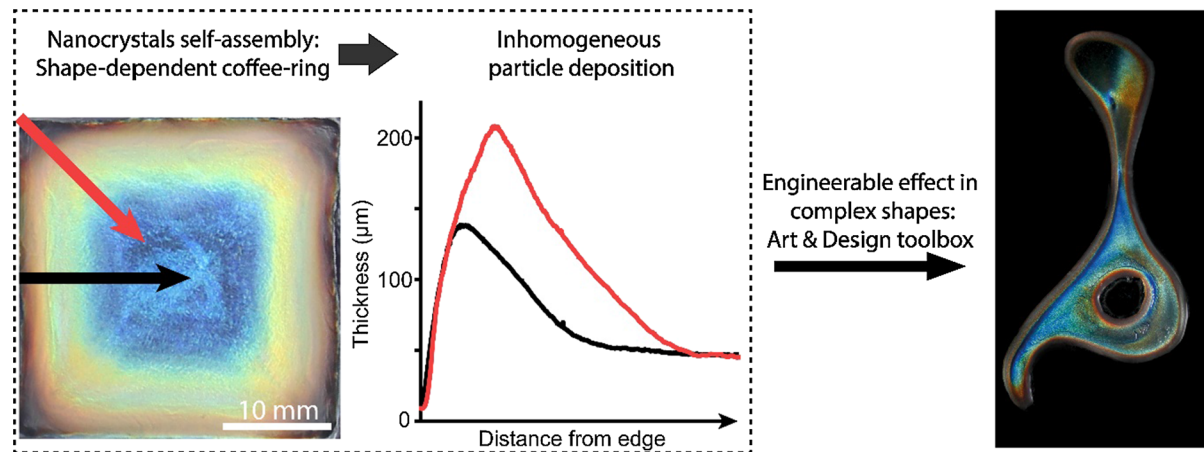
O. J. Rojas  
e-mail: orlando.rojas@aalto.fi

N. E. Yau · J. Beidler  
Color and Material Design, Department of Design, Aalto University, 00076 Aalto, Finland

E. Boutonnet  
CNRS, Grenoble INP, LGP2, University Grenoble Alpes, 38000 Grenoble, France

J. Beidler  
Converse Inc., Lovejoy Wharf 1, Boston, MA 02114, USA

## Graphical abstract



**Keywords** Cellulose nanocrystals · Coffee rings · Iridescence · Color fading · Art and design

## Introduction

It has been argued that interest in glittering objects originates not only from social reasons but also from evolutionary biases, some of which relate to the effects perceived when looking at fresh water. In nature, iridescence is associated with materials of high strength such as nacre, polished bone and soapstone (Meert et al. 2014). Besides its functional aspects, the “evolutionary bias” towards iridescence has resulted in a vast amount of ornamental designs. Growing interest in man-made iridescence is therefore not surprising. Indeed, shiny metallic colors appeal to the eyes and are used as special effects in visual industries, as shown in ceramics (Peterson and Peterson 2012) and glass (Eiseman et al. 2011) (see Fig. 1a for an exhibition of our own). The same is being realized in commodity products and fashion, as an answer to consumer needs and a growing trend. As a noteworthy example, active wear and footwear companies markedly increased the number of products with metallic effects in the year 2018 compared to the previous one (Fig. 1b), according to commerce data generated via web crawlers and artificial intelligence (Edited 2018). Moreover, forecasts from the Worth Global Style Network (WGSN) (Bailey et al. 2018) highlight “glitter”, “holography” and “iridescence” as future

tendencies in fashion, food, cosmetics and interior design, using databases with facts, figures and images for real-time retail coverage, trend analyses, consumer research and business information.

While there is an evident economic impact in exploiting iridescence as an optical property, consumers have become more environmentally-responsible and value the lifecycle and carbon footprint of consumables. This is documented for the younger generations (Generation Z) (Masdar 2016). For instance, solutions to the growing microplastic pollution in oceans (Law and Thompson 2014) and climate change are sought after. Therefore, there is an obvious need to use sustainable alternatives to the components currently used to produce metallic, shiny and iridescent effects, manufactured so far mainly from combinations of metals, silica and plastics (Maile et al. 2005). There is also a recent emphasis on the environmental impact of post-consumer waste from small disposables, including single-use plastic straws (MacArthur 2017) and others.

In the context of consumer needs and environmental consciousness, designers and researchers are well positioned to combine biobased materials and color designs as an answer to the demand of “glittery” products. As such, the present discussion is a result of the dialogue between aestheticism and functionality, which can be best exemplified in efforts to engineer optical reflections (Fig. 1c, d).

One of the most promising material sources toward bio-based iridescence are plant-based cellulose nanocrystals (CNCs), when used in solid films and

coatings (Habibi et al. 2010; Abitbol and Cranston 2014; Lagerwall et al. 2014). The highly crystalline, rod-like CNCs self-assemble above a critical concentration (Revol et al. 1992) into nematic layers with an inter-layer twisting angle that produces helical chiral nematic (cholesteric) liquid crystal phases. Upon drying, the suspension undergoes evaporation-induced self-assembly (EISA), and produces structural color in the dry films if the time for self-assembly between the critical and gelation concentrations is long enough (Mu and Gray 2014). The pitch, defined as the distance for a 360° twist of the nematic layers, determines the color that the dry film reflects, in addition to the tilt of the chiral nematic axis respective to the light source (Dumanli et al. 2014). The drying of the CNC suspension also results in the well-known “coffee ring” effect, whereby individual CNCs move preferentially towards the edges (Mu and Gray 2015) (see Fig. 1c, d). This is a consequence of capillary flow induced by the gradient of solvent evaporation rates across the drying film (Deegan et al. 1997). As a result, a gradient in CNC particle density occurs along the meniscus. This effect is often counteracted by the liquid flow, following the Marangoni effect, as a result of surface tension gradients created by differences in concentration or temperature (Hu and Larson 2006; Gençer et al. 2017). In a typical coffee ring, a broad range of distinctive colors are reflected as a function of the distance from the drying edge, where the material away from the edge produces a more homogeneous assembly, and hence, color. For large scale production of structurally colored materials, the coffee ring is seen as a burdensome inhomogeneity impairing our perception of functional aspects (Cui et al. 2012a, b; Majumder et al. 2012; Gençer et al. 2018). However, in the context of art and design applications, this effect could be of great value for highlighting material and edges from a single “paint/colorant” suspension, especially if it yields iridescence spanning the whole color spectrum. Therefore, applications can be envisioned for the highly interesting visual features differentiating shapes, patterns and details, for example, in logos where structural color from coffee rings may be visually appealing. Interestingly, creating such effects with shiny or metallic impressions are otherwise extremely challenging to accomplish with traditional coloring methods. Thus, CNC self-assembly

offers an environmental and natural way to create chromatic effects for design applications (Fig. 1a, c, d).

While edge-highlighting effects are appealing for design applications, the literature has so far ignored the consequence of drying flux on non-circular, asymmetrical contours, which are more commonly encountered outside scientific inquiries (Fig. 1a, c, d). As the name indicates, the coffee ring effect refers almost exclusively to sessile drops with circular symmetry (Mu and Gray 2015; Gençer et al. 2017, 2018; Chu et al. 2018). The fitting of asymmetry in the coffee ring development entice fundamental scientific inquiries that, simultaneously, may have far reaching applications in design, visual arts and related industries.

In this work, we characterize the impact of capillary flow induced inhomogeneities onto non-strictly circular boundaries during EISA of CNC suspensions. Because pristine CNC films are brittle and significantly affected by drying stresses, we used a plasticizer in most instances, poly(ethylene glycol) (PEG). For simplicity, the edge-induced deposition of the colloids is herein referred to as “coffee ring”, as this has been the standard terminology used during the last two decades, although geometries formed in this work are different from the classical ones and may be otherwise more accurately described as “coffee rims”. The term is hereafter italicized to indicate the pseudo-circular nature of the effect. We characterize *coffee ring* distances as a function of surface area and sharpness of the features of the contour used, depending on the angle amplitude at the vertex in a planar geometry. Orientation-dependent contact angle measurements, profilometry and fixed-light source photography are carried out to demonstrate how particulate flux, which is induced by capillary flow and solvent evaporation, has a more prominent role in the case of more acute angles. The experimental results are coupled with numerical determination of drying fluxes using a three-dimensional (3D) model of a sessile drop placed onto a square surface.

Lastly, we address two relevant aspects of iridescence from CNCs: the effect of background color and resistance to fading. The effect of the background is emphasized by using a highly reflective (white paper) and non-reflecting (black textile) surface. We study

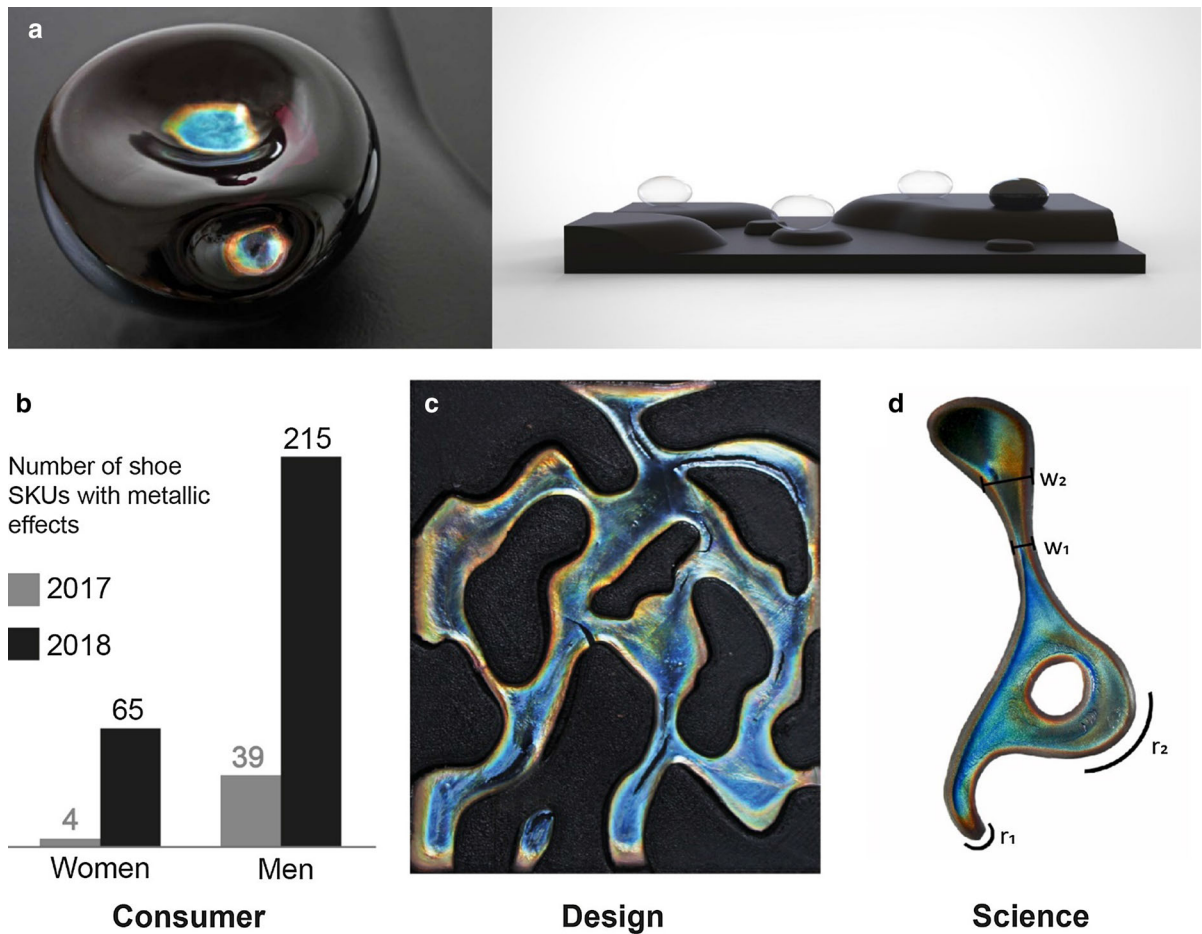


**Fig. 1** Multidisciplinary demonstration of consumer, design and science collaboration on CNC iridescent films towards applications in design and art. In nature, iridescence is used by living matter for a vast set of optical and mechanical functionalities (Parker 2000; Doucet and Meadows 2009). **a** Here we show how aesthetic visuals are generated on curved mouth blown glass objects (Yau 2017) to highlight the shapes by displaying different colors depending on the angle of observation. Another recent CNC-based art exhibitions can be noted (Abitbol et al. 2017). **b** Active wear and footwear companies

structural color fading in CNC films under a simulated sun (20% UV, 100% visible light compared to global, AM1.5G, standard spectrum) during a 6-week exposure. This corresponds to an exposure time under visible sunlight for 6 months in central European latitudes. The fading resistance of structural color from CNCs is demonstrated and compared to that of commercial standards, comprising textiles dyed to varying degrees (European Committee For Standardization 2014).

release a growing number of products (SKUs, or stock keeping units, refers to the number of products available for sale) that contain metallic effects in 2018 compared to 2017 (Edited 2018), emphasizing on increased consumer market demand. **c** Design produced from a 3D-printed mold to explore unique visual effects of CNCs generating *coffee rings* to highlight complex shape edges. **d** Details of *coffee ring* features for non-trivial alteration of feature width ( $w$ ) and in-plane radii of curvatures ( $r$ ). A wider *coffee ring* is formed at  $r_1$  when  $r_1 < r_2$ , whereas a wider *coffee ring* is formed at  $w_2$  when  $w_2 > w_1$

## Experimental

### Materials

Cellulose nanocrystals (CNCs) were produced at the USDA Forest Products Laboratory (FPL, Madison, WI) and obtained from the Process Development Center in the University of Maine. They were received as a suspension at 11.1% solids concentration. Details about the CNCs are listed in previous work (Klockars et al. 2018). Ethanol (A, 94%) was obtained from Altia

Oyj and poly(ethylene glycol) (PEG) (10 kDa) was obtained from Sigma-Aldrich. Millipore (Synergy UV) Milli-Q water was used to dissolve PEG and dilute the CNC suspensions.

### CNC film development

The 11.1% CNC suspension was diluted to 5.55% (w/w) using PEG aqueous solution. The PEG-containing suspensions are referred to according to the PEG content with respect to the total CNC solids (w/w), namely 0%, 15% and 60%. Cut-outs with specific shapes were made on Bemis Parafilm sheets (127  $\mu\text{m}$  thick). The paraffin sheets were pressed thoroughly on top of glass substrates that were first washed with ethanol. CNC suspensions containing varying amounts of PEG were cast on top of the glass slides, inside the open space surrounded by the paraffin film, so that this area was wetted by the fluid. All cast areas contained 0.22 mL  $\text{cm}^{-2}$ , corresponding to 12.21 mg of CNC  $\text{cm}^{-2}$ . Additionally, CNC suspensions were cast on flat 30  $\times$  30  $\times$  0.3 mm<sup>3</sup> Nylon sheets. The ratio between suspension volume and film cast area was kept constant, 0.22 mL  $\text{cm}^{-2}$ . In this way the average thickness of all the films was also constant. Solid films were obtained by letting the suspension dry for at least 50 h at 50% relative humidity and 23 °C. The topography of the films was mapped with a Dektak 6 M profilometer. Measurements were carried out at a 0.6 mm/s rate and using constant pressure equivalent to a 3 mg tip weight.

### Evaporation rate modelling

Surface Evolver 2.70 (Brakke 1992) was used to evaluate the shape of minimum energy, under gravity and surface tension forces, formed by a droplet of water bound by a square contact line (22  $\times$  22 mm<sup>2</sup>) at 23 °C. The given surface topography that resulted from energy minimization was incorporated in the definition of the solution domain of the steady-state diffusion equation for the concentration of water vapor,  $\nabla^2 c(\vec{r}) = 0$ , which was solved numerically in COMSOL Multiphysics 5.3a using the saturation vapor concentration  $c = 1$  and ambient vapor concentration,  $c = 0.5$  (at 50% relative humidity), as the boundary conditions at the meniscus and far from the liquid phase, respectively. The evaporative flux over

the meniscus was calculated from  $\vec{J}(\vec{r}) = -D\nabla c(\vec{r})$ , where  $D$  is the diffusion coefficient of water vapor in air (Deegan et al. 1997). The local evaporative volume loss  $dV_e = \frac{\Delta t}{\rho} \vec{J}_0(\vec{r}) \cdot d\vec{A}$  over  $\Delta t = 60$  s was used to calculate the convective influx  $dV_c$  during the initial evaporation phase with an approximately constant evaporation rate. The influx was calculated using  $dV_{\Delta t} = dV_0 - dV_e + dV_c$ , where  $dV_0$  and  $dV_{\Delta t}$  correspond to the differential volume elements of a minimum energy droplet at  $t = 0$  and  $\Delta t$  with volumes  $V_0$  and  $V_{\Delta t} = V_0 - \int dV_e$ , respectively.

### Structural color and fading

The resistance to fading by exposure to visible and ultraviolet light was studied using CNC films that developed structural color upon EISA on glass Petri dishes (Brand 40  $\times$  12 mm<sup>2</sup>). The films were made by deposition of a neat 6% CNC suspension using a volume of 2 or 4 ml. Additional experiments were performed by using 4 ml of the CNC suspension in the presence of 35% PEG based on CNC dry mass. These samples were exposed to UV light and are denoted CNC<sub>thin</sub>, CNC<sub>thick</sub> and CNC<sub>PEG</sub>, respectively. Another identical set of samples were kept away from UV light and used as controls. Two sets of eight different blue wool standards were used as a reference to quantify the extent of fading for such materials bearing no structural color. One set was exposed to light, while the other was covered or kept away from light (European Committee For Standardization 2014).

The samples were placed in a solar simulator on a surface onto which light was shined from above. The light sources used in the testing were halogen lamps (Philips projection lamp, type 13117) providing 20% of UV light and 100% visible light regions compared with the AM1.5G standard Sun light spectrum. The detailed light spectrum of the simulator is indicated in the literature (Tiihonen et al. 2015). The temperature of the samples in the solar simulator was approximately 40 °C.

The exposed samples were photographed to track any color changes by using an Olympus E-620 digital camera with a resolution of 4032 by 3024. The samples were held in a black box placed on a light grey surface and illuminated with LED lamps equipped with light scattering films to obtain even lighting. The camera settings used in the photographing included

f/8.0 aperture, ISO100 sensitivity, 1/15 s shutter speed, RAW image type, and adobe RGB color space. A color checker passport was used to set both the white balance in the beginning of the photographing and the color palette for processing in the program Adobe Lightroom 3. With the program, the image format was changed from RAW to JPEG. The red, green, and blue pixel values were analyzed and plotted using Matlab. The CNC films prepared for the fading study were characterized with a PerkinElmer Lambda 950 UV–Vis spectrometer in transmission mode.

### Films imaging

A customized photography box was used to image all samples except for the ones pertaining to the fading experiments. The inside of the box was painted matte black to avoid internal reflection, and included an opening to fit the light source and camera. Once placed, they prevented any external light from entering the inside of the box. A tight-fitting JJC Macro LED circular light source was positioned around the camera lens. The film samples were placed inside the box and imaged with normal incident light. The reflected light was measured perpendicular to the film and camera lens. A Canon EOS 60D camera with a resolution of 5184 by 3456 was used for the photography. The distance between the camera/light-source to the center of the samples was kept constant at 21 cm. The *coffee ring* widths of the films were obtained through image analysis, by applying a black color mask on the images through ImageJ software (Default method). The mask included all RGB blue and green color values (0–255), and partially the RGB red colors (0–132). The widths of the *coffee rings* were obtained as the distance measured orthogonally (side) or diagonally (corner) from the film edge to the masked area.

## Results and discussion

### Coffee ring development in square films

Previous studies related to *coffee rings* from CNC suspensions consider circular shapes of fairly small areas (< 10 mm diameter), where the characteristics of the *coffee ring* is identical in all radial directions (Mu and Gray 2015; Gençer et al. 2018). However, the most

generic use of solid suspensions, including film casting and printing, involve the deposition on a substrate of more complex geometries, which may develop sharp edges with varying curvature. In this study, CNC films of different sizes and shapes were cast, while keeping the ratio of CNC suspension volume-per-unit-area constant. Figure 2 shows the effects of asymmetry, sharp edges and surface area of the films on the resulting color map. The contact line was pinned towards the paraffin wall during the evaporation of the sessile suspensions that proceeded to dry with a decreasing contact angle, as previously reported for circular sessile drops. Note that the paraffin did not play a significant role because of its non-wetting nature, as well as the low thickness compared to that of the gelling fluid (as confirmed by observing *coffee ring* development in dried sessile fluid pinned onto a free-standing squared surface, Fig. S2 online resource).

Figure 2a displays height profiles for the CNC film shown in Fig. 2b, measured orthogonally from the side, in the mid-section of the square (dotted lines in black, Fig. 2b). Included is also the profile in the diagonal direction, between the corner and the center point of the film (dotted lines in red, Fig. 2b). The photos added in Fig. 2a correspond to the regions measured in the film cuts. A higher film thickness is clearly observed near the edges, in agreement with observations for spheroidal sessile droplets (Mu and Gray 2015; Gençer et al. 2017), typical of the *coffee ring* effect (Deegan et al. 1997). The diagonal profile, measured between the corners of the square and the center, indicates a significantly larger height compared to the orthogonal profile (from the side to the center). Although the outer and inner slopes of both profiles are similar, the distance over which the *coffee ring* develops at the corner is significantly larger. This suggests a greater particle transport in the diagonal direction towards the corner of the drying fluid.

The central, flattened area of the film reflects in the blue spectrum of color and changes to green and then yellow at positions farther from the center (as the thickness of the film increases). The outer region of the *coffee ring* displays a distinctive reddish color, while moving further away from the location where the films are the thickest, an area is reached that does not reflect light. Thus, the profilometry height data and photography indicate that a correlation exists between color and film thickness (Fig. 2a). However, the onset of the non-horizontal height profile does not coincide with

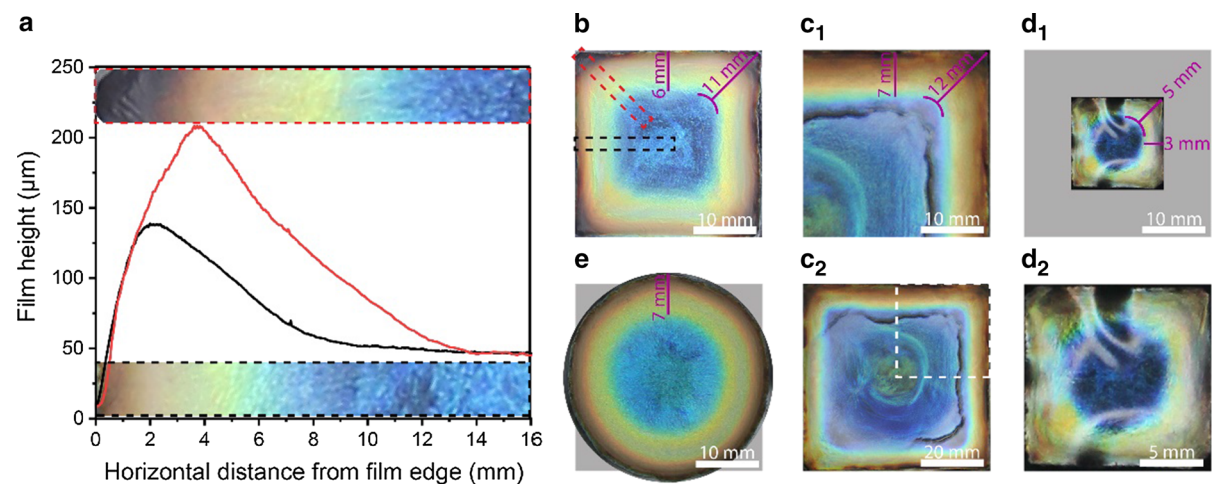


**Fig. 2** *Coffee ring* formation in CNC films of varying shape and size. **a** Height profile data (profilometry) on the areas corresponding to the photo image insets shown (see corresponding dotted rectangles in the film shown in **b**). The thickness variation is indicated from the side to the center (black profile), and from the corner to the center (diagonal, red profile). **b–d** Square CNC films (**b**  $30 \times 30 \text{ mm}^2$ , **c**  $60 \times 60 \text{ mm}^2$  and **d**  $15 \times 15 \text{ mm}^2$ ) containing 15% PEG. **e** Circular CNC film

the onset of the change in color from blue to turquoise (S1 online resource). Although the color of the film cannot be derived directly from its thickness, there is a trend towards a red shift for thicker films. The dimensions of the *coffee ring* in the square-shaped films show clear differences when comparing the corner and the side, which is apparent from both profilometry data (Fig. 2a) and color reflection (Fig. 2b–d). In contrast, the *coffee ring* is radially symmetric in a circular film (Fig. 2e), whereby the width of the *coffee ring* is the same along the circumferential edge (Mu and Gray 2015). We note that the distinctive reflected colors produced upon drying the CNC suspension correspond to both irradiation and observation normal to the plane. Thus, color capture at oblique angles would produce other results across the film height profile.

The films in this study were all dried at 50% relative humidity to improve reproducibility, and to ensure a longer evaporation time and, therefore, to favor chiral nematic assembly as well as *coffee ring* formation via EISA (Klockars et al. 2018; Tran et al. 2018). Otherwise, at high enough drying rates, “kinetic trapping or arrest” would occur for particles, limiting the formation of the *coffee ring* (Li et al. 2016). To briefly recapitulate, the phase transitions during EISA and ensuing *coffee rings*

(15% PEG) with a foot-print equal to the area of film (**b**). **c<sub>1</sub>** and **d<sub>1</sub>** are scaled to the same size as **b** and **e**, for easier visualization. The added curved purple lines are of equal size and curvature and indicate the same dimensional features for the three films (**b–d**). Purple lines are also added across the *coffee rings* to indicate their respective widths (note the dimensions given for the normal and diagonal direction). The average CNC mass per surface area was kept constant in all the films

can be described as follows: The chiral nematic liquid crystalline phase forms from a collection of merging spherical CNC assemblies or tactoids (Wang et al. 2016). During drying of the CNC suspension, the tactoids follow the capillary flow towards the edge (Chu et al. 2018), which is subjected to faster evaporation rates (Hu and Larson 2002). This results in tactoids that are kinetically confined at the air–water and water–substrate interfaces, with their chiral nematic axes also trapped at random orientations at the *coffee ring* edge (Hsiao et al. 2015). Previous studies on the effect of drying rate on color development indicated that disordered chiral nematic domains led to an increased pitch size and a red-shift, as well as a broad reflection spectrum (Beck et al. 2013; Natarajan et al. 2017). The apex height of the *coffee ring* reflects red-shifted colors due to a larger pitch, or a chiral nematic axis orientation non-perpendicular to the film plane (de Vries 1951). Closer to the center of the film, the solvent evaporates slower and the chiral nematic domains have more space and time to orient and display smaller pitch (Dumanli et al. 2014). Thus, the specific reflection wavelengths of the film change from green towards blue.

Square films of different size display a similar evolution of the reflected color, as is observed when moving from the center of the film towards the edge.

The smallest film was detached from the support during EISA, Fig. 2d, and was deformed due to drying stresses (Lee and Routh 2004; Zhou et al. 2006; Chekchaki and Lazarus 2013), which resulted in the shadowed areas in the image. In Fig. 2c, there are “valleys” within the film, which do not contain any solid material. They arise from larger drying stresses induced by the larger planar scale of the films compared to the smaller films (Fig. 2b, d) with similar thicknesses. Differences in the *coffee ring* width were noted for the square films at the side edges ( $W_{edge}$ ), using a color mask obtained via ImageJ. The *coffee ring* widths of the larger films (6 and 7 mm, respectively, Fig. 2b, c) were twice as large compared to that of the smallest film (Fig. 2d, 3 mm). In addition, the *coffee ring* shape of the larger films followed the square horizontal profile, which contrasts with the smallest film (Fig. 2d) that developed a circular *coffee ring* and blue area in the center. The observations indicate that in drying of CNC suspensions of small areas, the higher particle flux towards the corners is combined with the one towards the sides (Fig. 2d). In contrast, the outward radial fluxes for diagonal and lateral directions are decoupled in films of sufficiently large area. The critical film size for such flux decoupling is expected to occur when the *coffee ring* has reached a maximum width and follows the contact line at the square’s edges.

The *coffee ring* width was also measured at the corner ( $W_{corner}$ ), as the distance from the corner edge towards the center, until reaching the color threshold determined by the ImageJ color mask. Online resource Figure S1 indicates the positions in the film, and the corresponding thickness, which were used in determining  $W_{corner}$  and  $W_{edge}$ , based on the color mask. The threshold color is not based on any specifically relevant thickness or color, as the color change is continuous. Nevertheless, a non-arbitrary foundation for the comparison of *coffee-rings* can be established. The approximate ratio of coffee ring width at the corner and the edge ( $W_{corner}/Wedge_{edge}$ ) was calculated assuming the values shown in Fig. 2b–d. The ratios for the small, medium and large square films are 1.67, 1.83 and 1.71, respectively, i.e., relatively independent of size. It should be emphasized that all the  $W_{corner}$  values are larger than those caused purely by geometrical effects (longer distance to the center from the corner). Multiplying the  $W_{edge}$  values with the square root of two yields lower values than the

$W_{corner}$  value measured herein for all films. A closer observation of the corners in the larger films (Fig. 2b, c, upper images) reveals that the shape of the blue region is somewhat curved, with similar radii of curvature along the blue/green border (purple markers in Fig. 2b–d). Thus, CNC suspension drying near the corners is expected to be independent of the square size but rather depend on the film edge geometry. The CNC concentration (Klockars et al. 2018), as well as the drying rate (Beck et al. 2013; Natarajan et al. 2017) may further affect *coffee ring* formation.

#### Asymmetric drying gradients and effect on capillary flux

So far, the discussion has focused on experimental evidence of an increased deposition of CNCs towards the corners, as well as a larger *coffee ring* area. It is reasonable to propose that these effects arise from different capillary fluxes in square films under EISA, where the contact line is non-circular, and the meniscus is non-hemispheroidal. The square geometry may lead to spatial differences in drying rates along the meniscus, which in turn would cause different capillary flow from the center to the corners compared to that from the center to the sides. The non-trivial meniscus topography is evident in Fig. 3a according to the contact angles observed at different locations for a CNC aqueous suspension (1.08 mL, 5.5 wt%) pinned onto a  $22 \times 22 \text{ mm}^2$  square-cut glass (Fig. 3a right side). On the side edge, the contact angle of the pinned suspension is larger than at the corner. We recreated a 3D model of this system (Fig. 3b inset) by setting the minimum surface area as a boundary condition for water (0% CNC) pinned into a square shape. The left side of Fig. 3a includes the side- and corner-views of the model droplet, respectively, where the smaller contact angle at the corner is also apparent, corroborating the experimental measurement. For simplicity, the model used water (Fig. 3a left side) while the experiments used the actual CNC suspension without PEG (Fig. 3a right side). The contact angles of the 3D model are  $\sim 52^\circ$  at the side (Fig. 3a top) and  $\sim 4.5^\circ$  at the corner (Fig. 3a bottom).

The local evaporation rate along the meniscus was calculated for the 3D model, assuming equilibrium conditions. The length of the orthogonal vectors drawn on the surface scales with the spatial-dependent evaporation rate coupled with the relative humidity

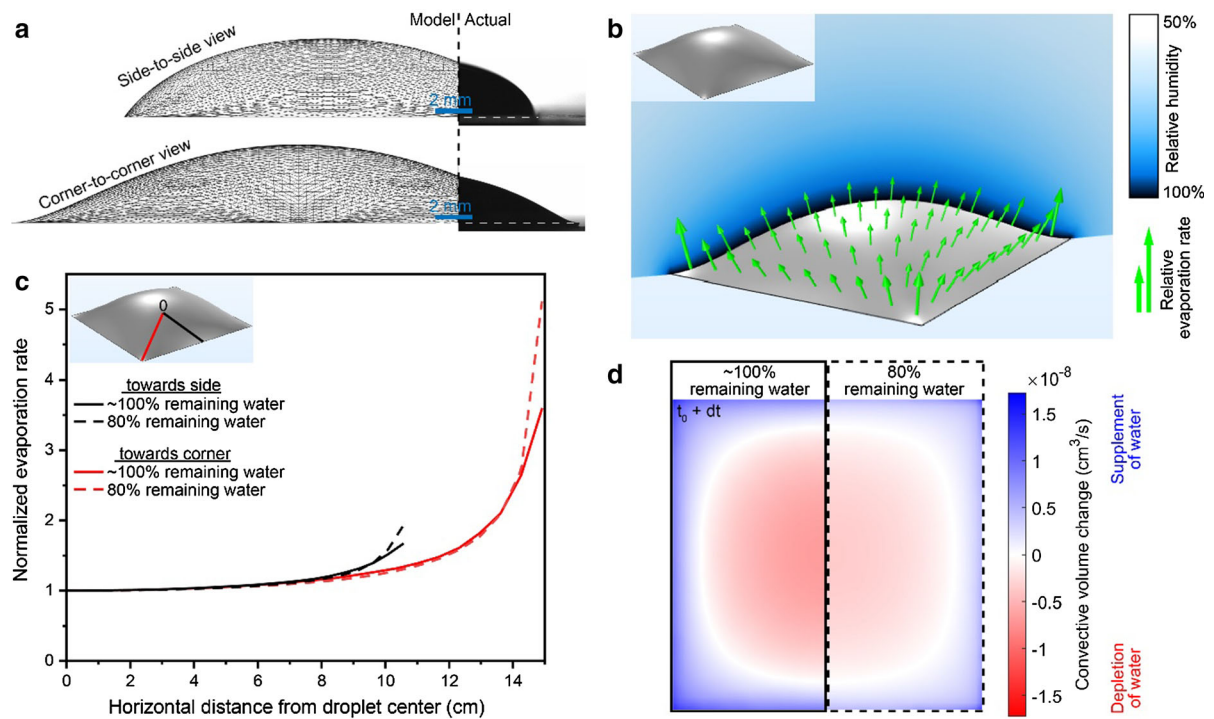


**Fig. 3** **a** Profile of a fluid volume on a surface according to a 3D model (left, 0% CNC), compared to the actual profile in the case of 1.08 ml of liquid wetting a  $22 \times 22$  mm $^2$  square-shaped area (right, 5.5% CNC). Images are shown from the side (top image) and corner (bottom image). **b** Modelled humidity gradient and local evaporation rates of the drying fluid at steady state conditions at the onset of the evaporation, as shown in the inset. **c** Calculated evaporation rates, going in the directions from the

center to the side (black line) or the corner (red line), when nearly 100% of the liquid remains (solid line), or when 80% of the liquid is remaining (dashed line). The values are normalized to the evaporation rate in the horizontal center. **d** Top view of the fluid volume, showing the change in the local water volume, under a period of 60 s. The left side corresponds to a 60 s period when 100% of the water is remaining, and the right side to a 60 s period after 20% of the water has evaporated

surrounding the droplet in Fig. 3b. At the center of the film, the flux is at minimum, as has been established before for circular droplets (Hu and Larson 2002). The model clearly shows that the water evaporation flux from the corner is greater than that from the side (Fig. 3c), suggesting a greater flux of water within the water volume towards the corners than towards the edges. The evaporation rate difference is even more pronounced at a time after 20% of the initial water volume has evaporated. Furthermore, this suggests an additional internal water flux from the center part of the edges towards the closest corners. Figure 3d indicates the local change in the areal (xy-plane) water volume after a time of 60 s. The values were calculated for two different times during the evaporation, where the left side corresponds to a time close to the start of the evaporation, while the right side describes a time when 20% of the water volume has been evaporated. The exceeding capillary flow

towards the corners suggests a relatively elevated deposition of CNCs in the corners, as shown earlier in the profilometry results of Fig. 2a.

#### Angle amplitude of non-circular films and effect on color reflection

We studied the effect of the angle amplitude at the corners of non-circular films on the *coffee ring* development by using geometries with increased sharpness, from 90° (squares) to 75°, 30° and 27.5°. Figure 4 shows CNC films with given amplitude angles, in which the width of the *coffee rings* was obtained using an ImageJ color mask, as per those in Fig. 2. The widths were the same for both the large triangular film shown in Fig. 4c–d, and the square film in Fig. 4a, even though the area of the triangle was 3.6 times larger. This result is not accidental but obeys our previous discussion on the “critical size” of the

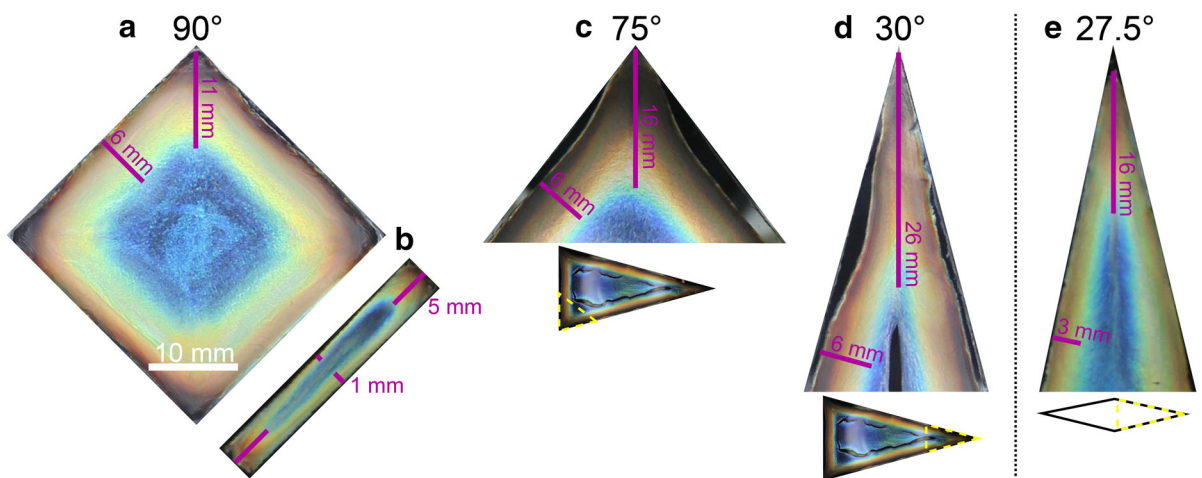


**Fig. 4** Films of varying corner angle amplitude developed from aqueous CNC suspensions with 15% PEG. The purple lines indicate the approximate *coffee ring* width. **a** 30 × 30 mm square-shaped film, also presented in Fig. 2b. **b** 30 × 5 mm rectangular film. A large triangular film (59-mm base and 110-mm height) is shown in the inset of **c**, **d**, where **c** shows the 75° corner, and **d** the smaller angle corner (30°). **e** Rhombus-

shaped film with an 85.8-mm long symmetry axis, and a 21-mm short symmetry axis. Only the upper half of the film is shown, corresponding to the dashed lines in the inset. All sizes are to scale, and the average CNC mass deposited per surface area was constant for all films. The purple distances measured in **b** are averages of the two corresponding distances

surface. For both shapes, the “critical size” has been reached, leading to decoupled flow towards the corners and the sides, and a maximum *coffee-ring* width. In contrast, for a CNC film (Fig. 4e) with an identical area but a different shape compared to the square film (Fig. 4a), the *coffee ring* width is reduced from 6 to 3 mm. Here, the size of the rhombus is smaller than its critical size, meaning that particle fluxes towards the corners and the sides are coupled. Therefore, the critical size depends not only on the area, but also on the shape of the film and the sharpness of the corners. In other words, films with a given area have reduced critical sizes for decreasing corner angle amplitudes. Interestingly, increasing the aspect ratio of a film with the same areal density of CNCs (Fig. 4b), produced similar *coffee ring* widths at the short side (6–5 mm), but significantly smaller ones (1 mm) along the long side (width ratio  $W_{short}/W_{long} = 5$ ). For a right angle, 90°, the  $W_{corner}/W_{edge} = 1.83$  while it was increased to 2.67, 4.33 and 5.33 for the more acute angles of 75°, 30° and 27.5°, respectively. The extreme boundary conditions would correspond to 180°, where the ratio is expected to tend to unity, and at an angle of ~ 0°, where the ratio would approach infinity. This emphasizes how the

combination of corner sharpness and aspect ratio can all be accessed to control the development of *coffee ring* highlighting at large scales. Here, it is worth noting that the  $W_{corner}$  values are larger than would be suggested simply from the geometrical diagonals for all the films. In other words, the measured values ( $W_{corner}$ : 11, 16, 26 and 16 mm, Fig. 4) are larger than the corresponding values obtained when normalizing the edge values to the additional distance to the corners: 8.5 (= 6 \* 2½), 9.9, 23.2 and 12.6 mm. The “valleys” within the film in Fig. 4c–d arise from larger drying stresses, as per those in Fig. 2c.

The discussion so far has been centered on the effect of surface geometry on the *coffee ring* effect, created by sessile volumes of CNC suspensions upon EISA. In the same vein, any application of CNCs to highlight the edges of given objects need to fulfil three ideal conditions, which are discussed in the next section: (a) understanding the effect of the optical properties of the solid support on the color reflected by the dried CNC films; (b) ensuring that cracking, which is typical of neat CNC films, is avoided by incorporation of plasticizers and, (c) achieving the long-lasting effects expected for structural color (non-fading reflections).

## Effect of background on perceived color reflection and permanency of structural color

We address two important benefits brought by CNC-based structural colors that, to our knowledge, have not been addressed in the literature so far. Namely, the effect of the background on the visual rendering of structural colors, and their non-fading property under light and heat. Comparing black and white backgrounds, significant effects have been described for the overall visual aspect of structural colors (Sakai et al. 2018). In the case of a black background, the colors observed result almost exclusively from the reflection inherent to the chiral nematic structure (Fig. S2 online resource). The use of a white background (Fig. S2 online resource) produces more complex effects since three phenomena superimpose: Reflections from (a) the CNC material, (b) the background and (c) colors reflected by the background that, in turn, are reflected by the CNC material. As the white background and the CNC film both reflect strongly, less intense colors are perceived against a white background under illumination (Sakai et al. 2018). As previously demonstrated, this can be used as an additional tool to exploit the interplay between related phenomena.

Normally, drying stresses in neat CNC films result in cracking, producing solid materials that are brittle and difficult to handle. The plasticizer added to the CNC suspensions prior to EISA (polyethylene glycol, PEG) enabled more flexible films with color shift towards red in the dry films, depending on the PEG content (Bardet et al. 2015; Gu et al. 2016; Yao et al. 2017). A PEG addition of 15% prevents crack formation while the blue color can be maintained (Fig. 5a, b). This is a consequence of the relaxation of the drying stresses by the presence of plasticizers that allow some level of molecular mobility (Lee and Routh 2004; Zhou et al. 2006; Chekchaki and Lazarus 2013). The insets of Fig. 5f, g show cracks in films produced in the absence of PEG, which were dried on glass substrates. In contrast, cracking was absent for the thin films shown in Fig. 5d, e (inset). A large PEG concentration, 60% (Fig. 5c) resulted in a red-shift (Yao et al. 2017), corroborating the possibility to tune colors depending on the composition. Interestingly, even when PEG was the dominant component of the dry material (60%), a clear iridescence could be observed, suggesting that the transition to isotropically

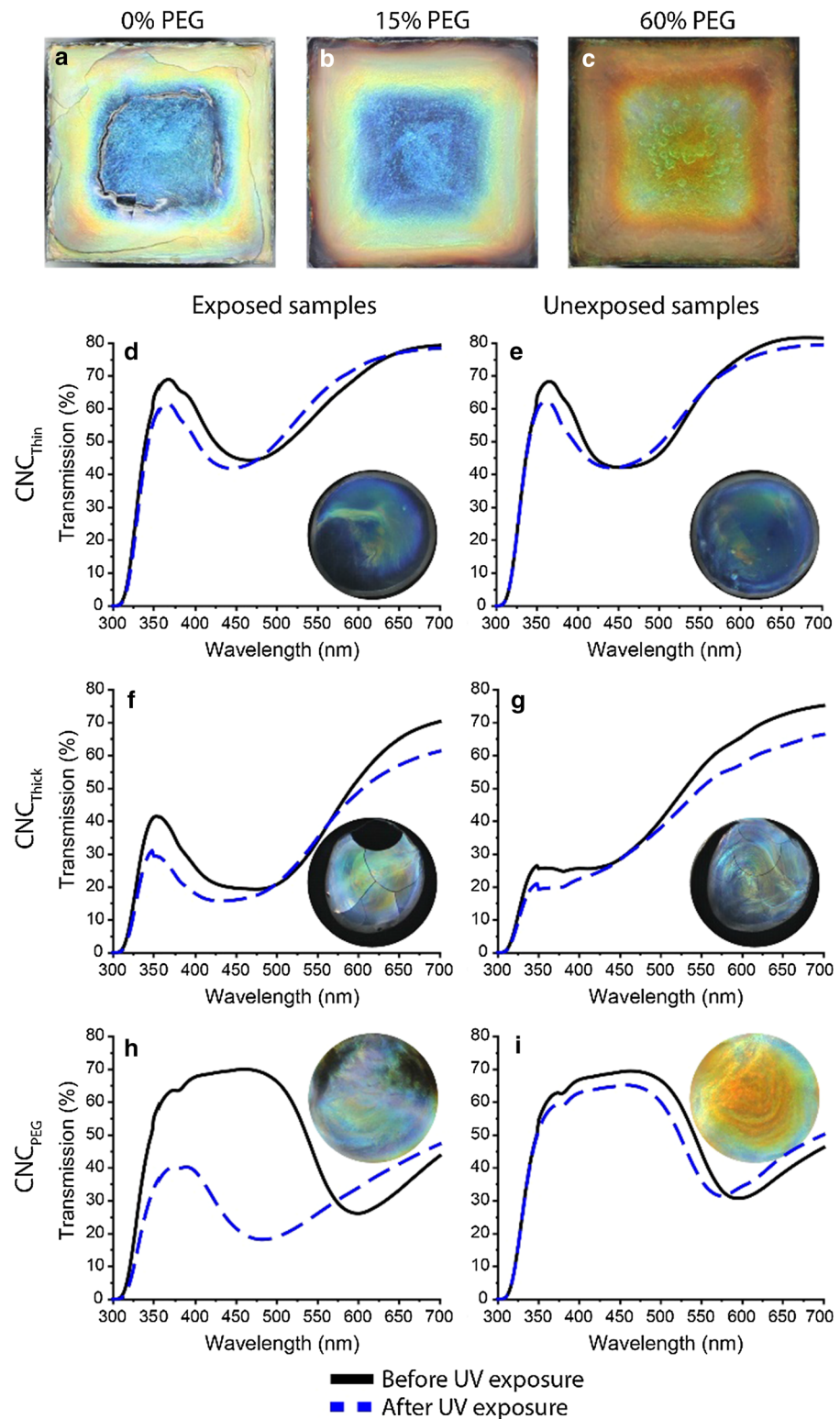
ordered CNCs would occur at higher concentrations of PEG. The same plasticizer has previously been observed to possess a low affinity to another lyotropic molecule, sunset yellow, instead coexisting with and mediating the formation of the liquid crystalline phase due to depletion effects (Park et al. 2011).

One important functionality of iridescent CNC films is the resistance to fading, an advantage over color derived from conventional dyes, which is crucial for achieving long-lasting effects. Art pieces and common objects both need regular maintenance and renovation due to loss of colors. Especially non-iridescent colors are prone to bleaching over time. Structural colors are produced as a result of nanostructures present at the reflecting surface (Kinoshita et al. 2008), unlike materials colored with dyes, where the color arises due to specific absorption from chemical components. Therefore, dyed or pigmented materials are considerably more susceptible to bleaching due to chemical degradation, for example, after exposure to UV-light. This contrasts with the structural color developed by CNCs, since any possible degradation will bear less consequences on the nanostructures than on a molecular dispersion of dyes. Therefore, structural colors offer considerable resistance to light exposure, and to some extent, also to heat.

The stability of the structural color to fading was tested in CNC films of two different thicknesses as well as in one set of films containing 35% PEG (based on dry CNC mass), by UV light exposure for a period of 6 weeks at 40 °C. In order to obtain quantitative proof of the fading resistance, UV–Vis spectroscopy was used to characterize the three different CNC films before and after the exposure (Fig. 5d, f, h). Another set of samples was kept away from light (stored in darkness) and were also characterized at the beginning and after 6 weeks (Fig. 5e, g, i). The insets in Fig. 5d–i show the films after light exposure. Considering the exposed CNC films, in the absence of plasticizer (Fig. 5d, f), the spectral minima are slightly shifted towards smaller wavelengths and the transmission intensity is reduced. However, these changes can be considered to be within the experimental error, since the unexposed counterparts displayed a similar trend (Fig. 5e, g).

There is a clear change in the reflection spectra for the CNC films containing PEG (Fig. 5h). In addition, there is a comparably smaller change in the spectra for

**Fig. 5** **a–c**  $30 \times 30 \text{ mm}^2$  square films obtained by EISA of aqueous suspensions of CNCs (5.5%) in the presence of various concentrations of PEG plasticizer relative to CNC mass, as indicated. **d–i** UV–Vis spectra for the samples tested for fading resistance, before and after UV exposure. Samples exposed continuously to UV light for 6 weeks are shown in **d, f, h**, while **e, g, i** correspond to non-exposed samples. The photographs added in each plot correspond to the films after exposure. The volume per unit area of the solid suspension to form the films was  $0.22 \text{ mL cm}^{-2}$  for the films in **a–c**, and  $0.21, 0.42$  and  $0.42 \text{ mL cm}^{-2}$  for **CNC}\_{\text{Thin}}** (**d–e**), **CNC}\_{\text{Thick}}** (**f–g**) and **CNC}\_{\text{PEG}}** (**h–i**). A 35% PEG content was used in **h–i**



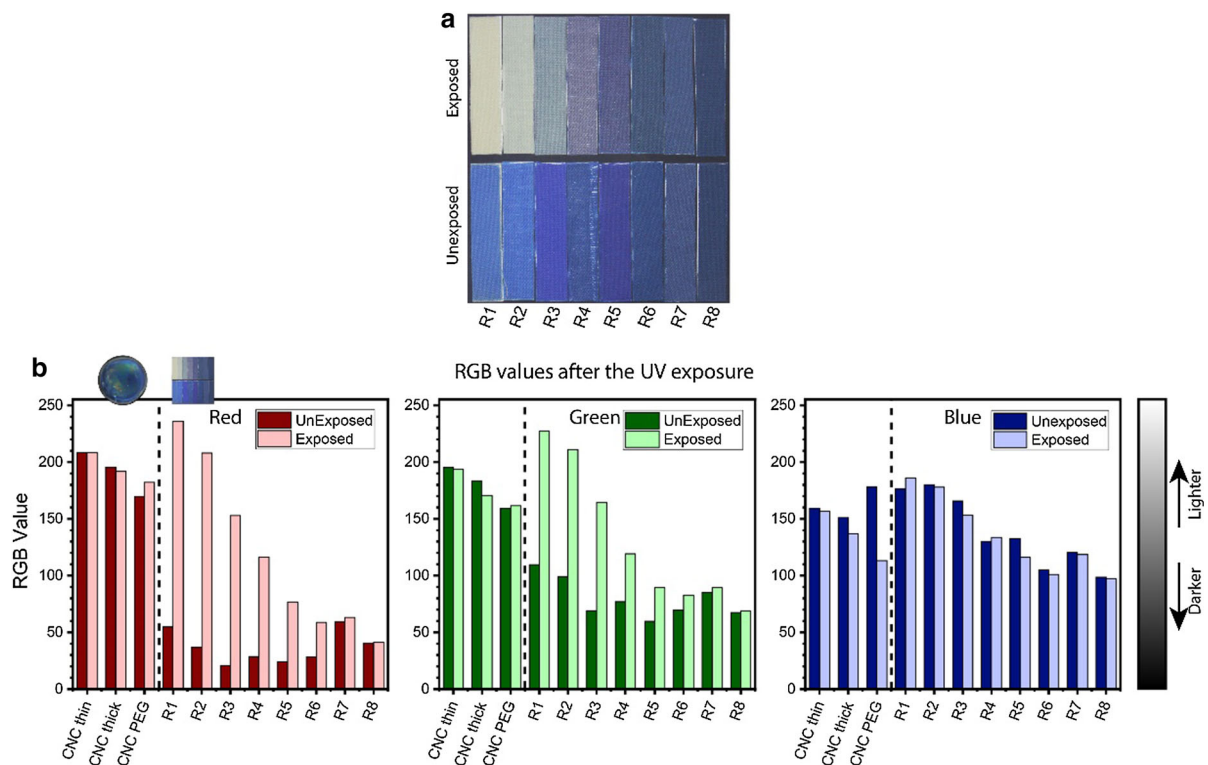


**Fig. 6** **a** Blue wool fading strips used as a reference for the extent of fading, where R1–R8 corresponds to the 1–8 grading scale (European Committee for Standardization 2014). The photo images of the upper eight strips were taken after UV light exposure for 6 weeks while the lower row corresponds to the eight strips that were kept away from light. **b** Image analysis of

the CNC samples shown in **d–i** and the blue wool fading strips from **a**, showing the separate absolute RGB color grading of each sample. The volume per unit area of the solid suspension to form the films was 0.21, 0.42 and 0.42 mL cm<sup>-2</sup> for CNC<sub>Thin</sub>, CNC<sub>Thick</sub> and CNC<sub>PEG</sub>

the unexposed CNC-PEG film (Fig. 5i), indicating that the change in color was due to the UV exposure. UV light chemically degrades PEG (Giroto et al. 2010), whereas CNCs also degrade as a result of oxidation-based stress as in photodegradation (Malešić et al. 2005), but are visibly less affected. A small loss in mass during the exposure of the CNC<sub>PEG</sub> film corresponded to one-third of the initial PEG mass, suggesting a loss of degradation products of PEG by evaporation. However, the results clearly indicate that the PEG is embedded within the pseudo-planes of the chiral nematic domains, and not only between the domains of chiral nematic order. As the PEG is degraded, the pseudo-planes approach each other and the pitch size shrinks, resulting in a reflection color that is blue-shifted (de Vries 1951). It might be interesting to conduct thermogravimetric analyses before and after UV-light exposure to quantify the overall degradation of cellulose, within the CNCs.

However, it is clear that the blue shift of the film upon degradation of PEG has nearly identical reflection properties as the native films, highlighting the strong UV-resistance of the CNC chiral nematic architecture in the film compared to that of the dispersed PEG molecules. The plasticizer can make CNC films more ductile and flexible while controlling the reflection color of the films but, on the other hand, significantly limits the UV-resistance of the assembly. This highlights a very important consideration for the future design of materials for photonics application using reflection from nano-scaled architectures.

Eight blue wool fading strips (R1–R8) were used as a reference material to evaluate the degree of fading exhibited by the CNC-based films. The former samples have known fading qualities, numerically described in grades from 1 to 8 as the resistance is increased. The fading resistance of CNC films is shown by image analysis performed on the photo

images of the CNC samples and the two sets of blue wool fading strips, from which one set was exposed while the other was kept in darkness (Fig. 6a). The RGB colors of the samples imaged after the exposure were processed with Adobe Lightroom 3 software and then analyzed using Matlab (Fig. 6b). Figure 6a shows that there is an apparent change in color of the strips up to that corresponding to number 6 (R6), where the color change is minor. The image analysis confirms this observation, as changes clearly occurred in the RGB red and green colors for all strips up to R6. Meanwhile, there is a very small change of color for the CNC samples, indicating fading resistance, in a grading scale similar to the standard under number 6. A change was evident in the RGB blue color for the CNC sample containing PEG, indicating a darkening of the blue color, which indicated the degradation of PEG, which is also visible in Fig. 5h. It is proposed that the visual output of the degradation of PEG could be utilized as photochromic timers, which could quantify the UV exposure duration via image analysis (Fig. 6) or UV–Vis spectroscopy (Fig. 5).

## Conclusions

In this study we address important challenges for the next generation of color designs and shine light on several unexplored aspects of particulate assembly under capillary flow. We studied the formation of coffee rings in non-circular CNC films, emphasizing the importance of the created highlight effect for art and design applications, where complex shapes are more common. We demonstrate that the casting area, with decreased size and, more importantly, increased contour sharpness, resulted in more pronounced and localized *coffee ring* effects. This corresponds to thicker film edges and longer distances over which the *coffee rings* would develop from more acute angles. We relate such effects to energy minimization during the drying of the suspension cast on non-circular geometries, and calculated vapor and capillary fluxes that lead to the inhomogeneous depositions of colloids around the contours of the sessile drops. We also characterize, for the first time, two other important benefits brought forward by CNC-based iridescence, namely the effect of background reflections and the UV-resistance of the structural colors. A continuous dialogue between material scientists and designers is

needed to further develop CNC-based structural colors towards product design and industrial manufacturing. Additionally, new methodologies for the use of CNC-based iridescence as “paint” are required in order to reduce drying times, which significantly reduces the potential of CNC-based iridescence in large-scale implementation. Also, coatings made from CNCs are susceptible to swelling and structural damage when exposed to water but this is addressable by application of water-resistant coatings, as exists for traditional coloring methods. The expanded fundamental understanding of CNC self-assembly may also benefit related goals, for example the development of coatings for fabrics (Tardy et al. 2017).

**Acknowledgments** Open access funding provided by Aalto University. The European Research Commission is thanked for support via ERC Advanced Grant 78848 “BioElCell”. We are also grateful to Aalto University Materials Platform for funding the MSc thesis of Noora Yau under the project LiCOS. The authors acknowledge the Academy of Finland through its Centres of Excellence Programme (2014–2019) under Project 264677 “Molecular Engineering of Biosynthetic Hybrid Materials Research” (HYBER) and the Aalto-VTT CERES Materials Bioeconomy Cluster funded by the Academy of Finland Flagship program. Kati Miettunen thanks Kone Foundation for its support.

## Compliance with ethical standards

**Conflict of interest** The authors declare that they have no conflict of interest.

**Open Access** This article is distributed under the terms of the Creative Commons Attribution 4.0 International License (<http://creativecommons.org/licenses/by/4.0/>), which permits unrestricted use, distribution, and reproduction in any medium, provided you give appropriate credit to the original author(s) and the source, provide a link to the Creative Commons license, and indicate if changes were made.

## References

- Abitbol T, Cranston ED (2014) Self-and direct-assembling of bionanomaterials. In: Handbook of green materials, vol 3. World Scientific, Singapore, pp 37–56
- Abitbol T, Shoval S, Blonder A (2017) Fleeting. In: Muza Eretz Isr. museum. <https://www.designboom.com/design/arielle-blonder-shira-shoval-art-piece-nanocellulose-eretz-israel-museum-09-27-2017/>; <https://materialdistrict.com/article/fleeting-nanocellulose-casted-iridescent-butterflies/>. Accessed 6 Dec 2018
- Bailey EG, Palmer H, Barnes O et al (2018) Beauty innovations: Korean packaging; surface and materials forecast S/S 20:

- code create; food and drink bites: April 2018; decorative accessories A/W 19/20: light magic. In: WGSN. <https://www.wgsn.com>. Accessed 30 Aug 2018
- Bardet R, Belgacem N, Bras J (2015) Flexibility and color monitoring of cellulose nanocrystal iridescent solid films using anionic or neutral polymers. *ACS Appl Mater Interfaces* 7:4010–4018. <https://doi.org/10.1021/am506786t>
- Beck S, Bouchard J, Chauve G, Berry R (2013) Controlled production of patterns in iridescent solid films of cellulose nanocrystals. *Cellulose* 20:1401–1411. <https://doi.org/10.1007/s10570-013-9888-4>
- Brakke KA (1992) The surface evolver. *Exp Math* 1:141–165. <https://doi.org/10.1080/10586458.1992.10504253>
- Chekchaki M, Lazarus V (2013) Mechanical stresses induced by evaporation in consolidated colloidal suspensions of hard particles. Poroelasticity theory versus experiments. *Transp Porous Media* 100:143–157. <https://doi.org/10.1007/s11242-013-0209-z>
- Chu G, Vilenky R, Vasiliev G et al (2018) Structure evolution and drying dynamics in sliding cholesteric cellulose nanocrystals. *J Phys Chem Lett* 9:1845–1851. <https://doi.org/10.1021/acs.jpclett.8b00670>
- Cui L, Zhang J, Zhang X et al (2012a) Suppression of the coffee ring effect by hydrosoluble polymer additives. *ACS Appl Mater Interfaces* 4:2775–2780. <https://doi.org/10.1021/am300423p>
- Cui L, Zhang J, Zhang X et al (2012b) Avoiding coffee ring structure based on hydrophobic silicon pillar arrays during single-drop evaporation. *Soft Matter* 8:10448. <https://doi.org/10.1039/c2sm26271a>
- de Vries H (1951) Rotatory power and other optical properties of certain liquid crystals. *Acta Crystallogr* 4:219–226
- Deegan RD, Bakajin O, Dupont TF et al (1997) Capillary flow as the cause of ring stains from dried liquid drops. *Nature* 389:827–829. <https://doi.org/10.1038/39827>
- Doucet SM, Meadows MG (2009) Iridescence: a functional perspective. *J R Soc Interface* 6:115–132. <https://doi.org/10.1098/rsif.2008.0395.focus>
- Dumanli AG, van der Kooij HM, Kamita G et al (2014) Digital color in cellulose nanocrystal films. *ACS Appl Mater Interfaces* 6:12302–12306. <https://doi.org/10.1021/am501995e>
- Edited (2018) Market analytics. <https://app.edited.com/>. Accessed 24 Jul 2018
- Eiseman L, Recker K (2011) Pantone (Firm) Pantone the 20th century in color. Chronicle Books, San Francisco
- European Committee For Standardization (2014) EN ISO 105-B02:2014 textiles—tests for colour fastness—part B02: colour fastness to artificial light: Xenon arc fading lamp test. p 3
- Gençer A, Schütz C, Thielemans W (2017) Influence of the particle concentration and marangoni flow on the formation of cellulose nanocrystal films. *Langmuir* 33:228–234. <https://doi.org/10.1021/acs.langmuir.6b03724>
- Gençer A, Van Rie J, Lombardo S et al (2018) Effect of gelation on the colloidal deposition of cellulose nanocrystal films. *Biomacromol* 19:3233–3243. <https://doi.org/10.1021/acs.biomac.8b00493>
- Giroto JA, Teixeira ACSC, Nascimento CAO, Guardani R (2010) Degradation of poly(ethylene glycol) in aqueous solution by photo-fenton and  $H_2O_2/UV$  processes. *Ind Eng Chem Res* 49:3200–3206. <https://doi.org/10.1021/ie9015792>
- Gu M, Jiang C, Liu D et al (2016) Cellulose nanocrystal/poly(ethylene glycol) composite as an iridescent coating on polymer substrates: structure-color and interface adhesion. *ACS Appl Mater Interfaces* 8:32565–32573. <https://doi.org/10.1021/acsmami.6b12044>
- Habibi Y, Lucia LA, Rojas OJ (2010) Cellulose nanocrystals: chemistry, self-assembly, and applications. *Chem Rev* 110:3479–3500. <https://doi.org/10.1021/cr900339w>
- Hsiao Y-C, Sung Y-C, Lee M-J, Lee W (2015) Highly sensitive color-indicating and quantitative biosensor based on cholesteric liquid crystal. *Biomed Opt Express* 6:5033–5038. <https://doi.org/10.1364/BOE.6.005033>
- Hu H, Larson RG (2002) Evaporation of a sessile droplet on a substrate. *J Phys Chem B* 106:1334–1344. <https://doi.org/10.1021/jp0118322>
- Hu H, Larson RG (2006) Marangoni effect reverses coffee-ring depositions. *J Phys Chem B* 110:7090–7094. <https://doi.org/10.1021/JP0609232>
- Kinoshita S, Yoshioka S, Miyazaki J (2008) Physics of structural colors. *Rep Prog Phys* 71:076401. <https://doi.org/10.1088/0034-4885/71/7/076401>
- Klockars KW, Tardy BL, Borghei M et al (2018) Effect of anisotropy of cellulose nanocrystal suspensions on stratification, domain structure formation, and structural colors. *Biomacromol* 19:2931–2943. <https://doi.org/10.1021/acs.biomac.8b00497>
- Lagerwall JPF, Schütz C, Salajkova M et al (2014) Cellulose nanocrystal-based materials: from liquid crystal self-assembly and glass formation to multifunctional thin films. *NPG Asia Mater* 6:80. <https://doi.org/10.1038/am.2013.69>
- Law KL, Thompson RC (2014) Microplastics in the seas. *Science* 345(80):144–145
- Lee WP, Routh\* AF (2004) Why do drying films crack? *Langmuir* 20:9885–9888. <https://doi.org/10.1021/LA049020V>
- Li Y, Yang Q, Li M, Song Y (2016) Rate-dependent interface capture beyond the coffee-ring effect. *Sci Rep* 6:24628. <https://doi.org/10.1038/srep24628>
- MacArthur E (2017) Beyond plastic waste. *Science* 80:358
- Maile FJ, Pfaff G, Reynders P (2005) Effect pigments—past, present and future. *Prog Org Coat* 54:150–163. <https://doi.org/10.1016/J.PORGCOAT.2005.07.003>
- Majumder M, Rendall CS, Eukel JA et al (2012) Overcoming the “coffee-stain” effect by compositional marangoni-flow-assisted drop-drying. *J Phys Chem B* 116:6536–6542. <https://doi.org/10.1021/jp3009628>
- Malesić J, Kolar J, Strlič M et al (2005) Photo-induced degradation of cellulose. *Polym Degrad Stab* 89:64–69. <https://doi.org/10.1016/J.POLYMDGRADSTAB.2005.01.003>
- Masdar (2016) The Masdar Gen Z global sustainability survey. <https://masdar.ae/en/initiatives/detail/about-the-masdar-gen-z-global-sustainability-survey>. Accessed 29 Aug 2018
- Meert K, Pandelaere M, Patrick VM (2014) Taking a shine to it: how the preference for glossy stems from an innate need for water. *J Consum Psychol* 24:195–206. <https://doi.org/10.1016/J.JCP.2013.12.005>
- Mu X, Gray DG (2014) Formation of chiral nematic films from cellulose nanocrystal suspensions is a two-stage process.

- Langmuir 30:9256–9260. <https://doi.org/10.1021/la501741r>
- Mu X, Gray DG (2015) Droplets of cellulose nanocrystal suspensions on drying give iridescent 3-D “coffee-stain” rings. *Cellulose* 22:1103–1107. <https://doi.org/10.1007/s10570-015-0569-3>
- Natarajan B, Emiroglu C, Obrzut J et al (2017) Dielectric Characterization of confined water in chiral cellulose nanocrystal films. *ACS Appl Mater Interfaces* 9:14222–14231. <https://doi.org/10.1021/acsmami.7b01674>
- Park H-S, Kang S-W, Tortora L et al (2011) Condensation of self-assembled lyotropic chromonic liquid crystal sunset yellow in aqueous solutions crowded with polyethylene glycol and doped with salt. *Langmuir* 27:4164–4175. <https://doi.org/10.1021/la200505y>
- Parker AR (2000) 515 million years of structural colour. *J Opt A Pure Appl Opt* 2:15–28. <https://doi.org/10.1088/1464-4258/2/6/201>
- Peterson S, Peterson J (2012) The craft and art of clay: a complete potter’s handbook. Laurence King Publishing, London
- Revol J-F, Bradford H, Giasson J et al (1992) Helicoidal self-ordering of cellulose microfibrils in aqueous suspension. *Int J Biol Macromol* 14:170–172
- Sakai M, Seki T, Takeoka Y (2018) Bioinspired color materials combining structural, dye, and background colors. *Small* 14:1800817. <https://doi.org/10.1002/smll.201800817>
- Tardy BL, Ago M, Guo J et al (2017) Optical properties of self-assembled cellulose nanocrystals films suspended at planar-symmetrical interfaces. *Small* 13:1702084. <https://doi.org/10.1002/smll.201702084>
- Tiihonen A, Miettunen K, Rendon S et al (2015) The effect of electrolyte purification on the performance and long-term stability of dye-sensitized solar cells. *J Electrochem Soc* 162:661–670. <https://doi.org/10.1149/2.0671509jes>
- Tran A, Hamad WY, MacLachlan MJ (2018) Tactoid annealing improves order in self-assembled cellulose nanocrystal films with chiral nematic structures. *Langmuir* 34:646–652. <https://doi.org/10.1021/acs.langmuir.7b03920>
- Wang P-X, Hamad WY, MacLachlan MJ (2016) Structure and transformation of tactoids in cellulose nanocrystal suspensions. *Nat Commun* 7:11515. <https://doi.org/10.1038/ncomms11515>
- Yao K, Meng Q, Bulone V, Zhou Q (2017) Flexible and responsive chiral nematic cellulose nanocrystal/poly(-ethylene glycol) composite films with uniform and tunable structural color. *Adv Mater* 29:1701323. <https://doi.org/10.1002/adma.201701323>
- Yau N (2017) Enter and encounter. In: Des. Museum. [http://www.designmuseum.fi/fi/exhibitions/enter\\_and\\_encounter/](http://www.designmuseum.fi/fi/exhibitions/enter_and_encounter/). Accessed 29 Aug 2018
- Zhou Z, Li Q, Zhao XS (2006) Evolution of interparticle capillary forces during drying of colloidal crystals. *Langmuir* 22:3692–3697. <https://doi.org/10.1021/LA052934C>